Giant crystalline anisotropic magnetoresistance in nonmagnetic perovskite oxide heterostructures

H. J. Harsan Ma,[1,2,3,4,*] J. Zhou,[2] M. Yang,[5] Y. Liu,[6] S. W. Zeng,[1,2] W. X. Zhou,[1,2] L. C. Zhang,[1,2] T. Venkatesan,[1,2] Y. P. Feng,[2] and Ariando [1,2,†]

[1]*NUSNNI-Nanocore, National University of Singapore, 117411 Singapore*

[2]*Department of Physics, National University of Singapore, 117542 Singapore*

[3]*Physikalisches Institut and Center for Quantum Science (CQ) in LISA+, Universität Tübingen, Auf der Morgenstelle 14, D-72076 Tübingen, Germany*

[4]*High-field Magnetic Resonance Center, Max Planck Institute for Biological Cybernetics, Speemannstraße 38-40, 72076 Tübingen, Germany*

[5]*Institute of Materials Research and Engineering, A*STAR, 2 Fusionopolis Way, 138634 Singapore*

[6]*Laboratoire Structures, Propriétés et Modélisation des Solides, CentraleSupélec, CNRS-UMR8580, Université Paris-Saclay, Grande Voie des Vignes, Châtenay-Malabry Cedex 92295, France*

(Received 3 October 2016; revised manuscript received 14 March 2017; published 20 April 2017)

Anisotropic magnetoresistance (AMR) was observed by Lord Kelvin one-and-half centuries ago in iron and nickel. The resistance of these ferromagnetic conductors showed a few percent change when a magnetic field was applied along or across the current. Subsequently, a 20% AMR was demonstrated in alloys of nickel and iron (permalloys). Efforts have then been devoted to extend this effect in multifunctional materials. The oxide heterostructure exhibiting two-dimensional electron liquid is one of the potential candidates as it has shown to exhibit emergent magnetic ordering, strong spin-orbit interactions, and anisotropic magnetoresistance. Here we show a giant crystalline AMR as large as 57% to 104% in anisotropic quantum wells based on nonmagnetic perovskite oxides $LaAlO_3$ and $SrTiO_3$, providing an alternative way in tailoring AMR with an extremely large effect. The AMR maximum appears when the magnetic field points along the in-plane $[1\bar{1}0]$ direction, irrespective of the direction of current flow, which is consistent with the idea of crystalline AMR. Data analysis and density functional theory calculation show that the observed giant crystalline AMR mainly originates from the strong anisotropic spin-orbit field at the interface due to its unique elliptical Fermi surface related to its orbital configuration and reconstruction. This work demonstrates that perovskite oxide interface is a unique platform for orbital physics.

DOI: 10.1103/PhysRevB.95.155314

I. INTRODUCTION

The emergent low dimensional electronic systems in perovskite oxide heterostructures built on strontium titanate are a relatively new class of electronic materials. A famous example is the observed metallicity [1] and two-dimensional (2D) superconductivity [2] at the interface between two insulating and nonmagnetic oxides $LaAlO_3$ (LAO) and $SrTiO_3$ (STO). The interface also hosts emergent magnetic [3–9] and spin-orbit [10–12] properties that are absent in the bulk constituents. In addition, the orbital states and spin-orbit interactions are tunable by an external electric field [10,11,13] and sensitive to the crystalline orientation [14–17]. It was shown that the itinerant d electrons which coexist with localized magnetic moments in this system can be gate tuned through a Lifshitz transition, where they change from populating light d_{xy} bands with a circular Fermi surface to occupying also heavy d_{xz}/d_{yz} bands with highly elongated elliptical Fermi surfaces oriented along crystalline axes [13,16]. The heavy d_{xz}/d_{yz} bands can have preferred axes for anisotropy along crystalline directions. The change of the Fermi surface by applying an electric field gate produces interesting phenomena such as gate-tuned polarized phases, which have been explored by measuring anisotropic magnetoresistance (AMR) [13,18–20]. This tunability provides a degree of control unattainable in conventional semiconductors, making oxide heterostructures ideal for electron spin/orbital-polarized injection and electric field devices [13,21].

AMR is a response of carriers in magnetic materials to changes of the magnetization direction [22–25]. It can be decomposed into two parts, one is a noncrystalline term, arising from the lower symmetry for a specific current direction, and another is usually much weaker crystal symmetry-related crystalline terms [26–28]. Earlier works on AMR in LAO/STO(001) system have addressed the effects of Rashba spin-orbit interactions and magnetic order [13,18,19]. AMR in LAO/STO(001) is usually dominated by a noncrystalline term which can be understood in the context of spin-orbit interaction. In this case, the anisotropy and maximum of the AMR depend on the current flow direction, namely, the position of the AMR maximum changes with the current flow direction. The crystalline AMR on the other hand has symmetry of the crystal structure, independent of the current direction. It was found that there is a relatively small crystalline AMR term emerging when one applies large magnetic field at low temperatures for high carrier density LAO/STO(001) samples, which could be achieved by electric field gating [13]. The appearance of the crystalline symmetry might be assigned to a change between d_{xy} band occupation with an isotropic Fermi surface, to the population of d_{xz}/d_{yz} orbitals with elliptical Fermi surfaces oriented along crystalline axes [13,29].

Here we demonstrate a giant crystalline AMR in (110)-oriented 10 unit cells LAO grown on STO [LAO/STO(110), methods section], which is different than the ordinary magnetoresistance or spin-orbit coupling induced

*harsanmhj@gmail.com
†ariando@nus.edu.sg

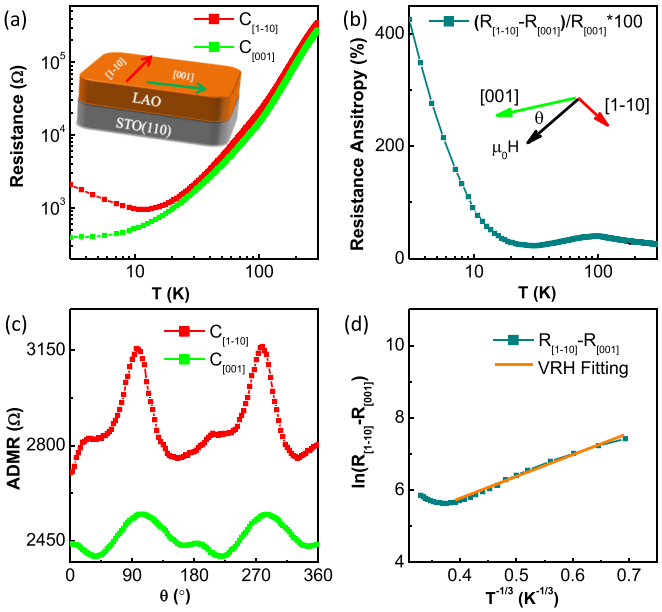

FIG. 1. Transport properties and anisotropic magnetoresistance (AMR) at $LaAlO_3/SrTiO_3$ (LAO/STO) (110) heterostructures. (a) Resistance as a function of temperature measured in the annealed LAO/STO (110) sample in the current along $[1\bar{1}0]$-orientated Hall bar ($C_{[1-10]}$) and in the current along [001]-orientated Hall bar ($C_{[001]}$) geometries showing resistance upturn at low temperatures for $C_{[1-10]}$. Inset shows a sketch of stack and transport measurement geometries. (b) Resistance anisotropic defined by $(R_{[1-10]}/R_{[001]} - 1)*100\%$ as a function of temperature for data shown in (a). Inset shows a sketch of definition of angle θ, which is the angle between magnetic field and [001] direction. (c) Magnetoresistance measurement in an in-plane rotating magnetic field of 9 T in $[1\bar{1}0]$- and [001]-orientated Hall bars with the angles defiend in (b). (d) The $\ln(R_{[1-10]}/R_{[001]})$ vs $T^{-1/3}$ plot for LAO/STO (110) sample and a 2D variable range hopping (VRH) fit.

noncrystalline term dominated AMR usually observed in (001)-oriented LAO/STO [13,18,19,30] or magnetic materials [31].

II. EXPERIMENT

The LAO/STO(110) heterostructures were prepared by pulsed laser deposition (PLD), ablating $LaAlO_3$ (LAO) target onto TiO_2-terminated $SrTiO_3$ (STO)(110) substrates. The laser (248 nm) energy density was $1.4\,J/cm^2$ and the repetition rate was 2 Hz. Samples with 10 unit cell LAO were grown on STO(110) single crystal substrates under oxygen partial pressure P_{O2} of 5×10^{-3}, 1×10^{-3}, 5×10^{-4}, and 5×10^{-5} Torr. The samples were annealed for 3 h at 1050 °C in air. Hall bars along two different directions [001] and $[1\bar{1}0]$ were defined by structuring the LAO layer using photolithography to dimensions of $50\times165\,\mu m^2$. The in-plane magnetoresistance measurement was performed by applying magnetic field parallel to the plane of the sample surface using a physical property measurement system as shown schematically in Fig. 1(a).

TABLE I. Maximum AMR signals with magnetic field of 9 T at 5 K for different samples with [001]- and $[1\bar{1}0]$-orientated Hall bars. Samples are all 10 unit cells LAO on STO(110) substrates, with different growth oxygen partial pressure.

	Sample growth pressure (10^{-4} Torr)			
Hall bar	50	10	5	0.5
$C_{[001]}$	6.5%	20%	16%	40%
$C_{[1-10]}$	16.8%	57%	69%	104%

III. RESULTS

A. Angle dependent anisotropic magnetoresistance

The two-dimensional electron liquid in LAO/STO(110) has been proven to be very anisotropic due to the reduced STO lattice symmetry C_{2v} in contrast to C_4 for LAO/STO(001) [14,16,17]. The sample is shown schematically in Fig. 1(a), inset. The current along the $[1\bar{1}0]$ is denoted by $C_{[1-10]}$ while along the [001] by $C_{[001]}$. The sample showed here is grown at oxygen partial pressure $P_{O2}=5\times10^{-3}$ Torr. Figure 1(a) shows resistance versus temperature showing a monotonic decrease with temperature along [001] and a low temperature upturn along $[1\bar{1}0]$, which can be fitted by 2D variable range hopping [27] [Figs. 1(b) and 1(d)]. Figure 1(c) shows the angle dependent in-plane AMR with θ defined as the angle between the magnetic field and [001] direction of the crystal measured at 5 K [Fig. 1(b), inset]. In both cases, the AMRs vary with θ and show maxima at $\sim90^\circ$ or 270°, namely, along $[1\bar{1}0]$ direction, which indicates dominating crystalline AMR. In contrast, the AMR observed in LAO/STO(001) systems showed a maximum when the current flow direction is perpendicular to the magnetic field for either current along [100] or [010] direction [13,18,19,30], which are not distinguishable in (001)-orientated interfaces, though there are some crystalline contributions when one applies large magnetic field at low temperatures for large carrier density samples [32,33].

B. Temperature dependent anisotropic magnetoresistance

Figures 2(a)–2(f) show temperature dependent AMR with a 9 T in-plane magnetic field for a different sample, 10 unit cells LAO/STO(110) grown at oxygen partial-pressure P_{O2} of 10^{-3} Torr. Regarding samples and reproducibility of the data, we have at least four samples containing four devices each patterned by photolithography. The AMR along $[1\bar{1}0]$ increases from 10% to 60% [Figs. 2(a), 2(c), and 2(e)] while along [001] from 5% to 20% [Figs. 2(b), 2(d), and 2(f)] with decreasing temperature from 20 to 5 K. The AMR is mostly positive and in both cases its maximum always appears at $\theta\sim90^\circ$ or 270°, namely, when the field is parallel to $[1\bar{1}0]$ direction. In other words, the global maximum AMR appears at a magnetic field parallel to $C_{[1-10]}$. Interestingly, the 60% AMR found here is tenfold larger than that in magnetic materials such as (Ga,Mn)As [31]. Moreover, the maximum AMR reach 104% for $C_{[1-10]}$ and 40% for $C_{[001]}$ for the sample grown at $P_{O2}=5\times10^{-5}$ Torr (Table I and Fig. 7). This giant crystalline AMR indicates a strong anisotropy in LAO/STO(110) compared to LAO/STO(001), which is related

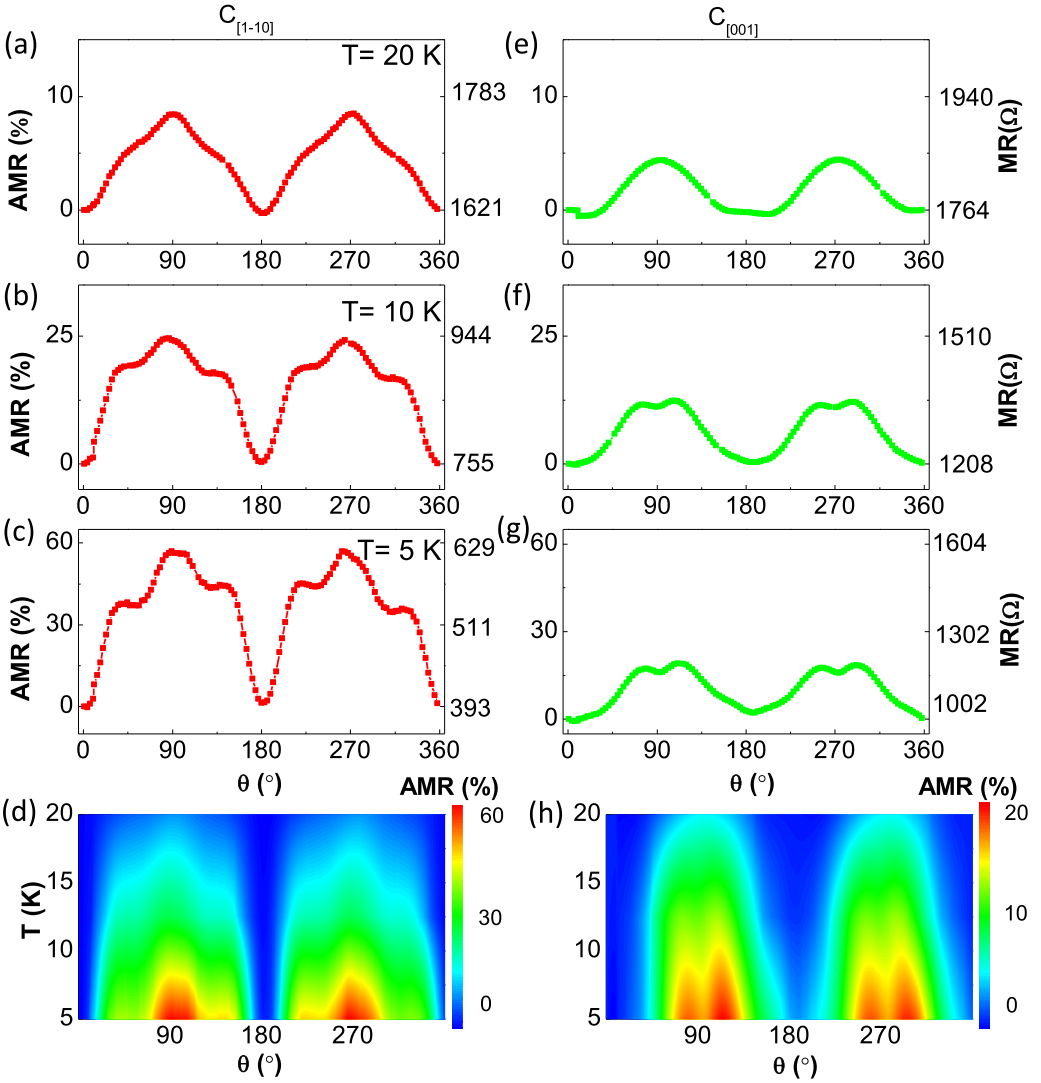

FIG. 2. Temperature dependent anisotropic magnetoresistance (AMR) signals of [1$\bar{1}$0]- and [001]-orientated Hall bars with an in-plane rotating magnetic field of 9 T. The angle is fixed according to the sample orientation. $\theta = 0^\circ$ is for magnetic field along [001] and $\theta = 90^\circ$ for [1$\bar{1}$0]. (a), (c), and (e) In [1$\bar{1}$0]-orientated Hall bar, we observe an increasing AMR signal up to 60% with decreasing temperature. The AMR signal is mostly positive and the maximum AMR always appears at θ close to or equal 90° or 270°, namely, when the magnetic field is parallel to [1–10] direction. The maximum AMR appears at magnetic field parallel to current direction. The corresponding raw magnetoresistance data are shown in the right axis in each figure. (g) AMR map of [1$\bar{1}$0]-orientated Hall bar for the entire temperature range below 20 K. (b), (d), and (f) In [001]-orientated Hall bar, we observe an increasing AMR signal up to 20% with decreasing temperature. The AMR signal is mostly positive and the maximum AMR always appears at θ close to or equal 90° or 270°, namely, when the magnetic field is parallel to [1$\bar{1}$0] direction. The maximum AMR appears at magnetic field perpendicular to current direction. The corresponding raw magnetoresistance data are shown in the right axis in each figure. (h) AMR map of [001]-orientated Hall bar for the entire temperature range below 20 K.

to the local orbital configurations and Ti-site symmetries. Figures 2(g) and 2(h) show the AMR map of $C_{[1-10]}$ and $C_{[001]}$ from 5 to 20 K, respectively.

Ferromagnetic metals exhibiting a normal AMR usually show maximum resistivity when the current is parallel to the magnetization direction $\boldsymbol{I}//\boldsymbol{M}$, and minimum resistivity when the current is perpendicular to the magnetization direction $\boldsymbol{I}\perp\boldsymbol{M}$. In the presence of Rashba type spin-orbit coupling, the sign of AMR flips. The global maxima of AMR appearing at 90° or 270° for both $C_{[1-10]}$ and $C_{[001]}$ were not observed in LAO/STO(100) system [13,18,19,30], in which the maxima appeared only when the current is perpendicular to the applied magnetic field. This crystalline AMR behavior observed in LAO/STO(110) is not expected from $\boldsymbol{k}\cdot\boldsymbol{p}$ Kohn-Luttinger Hamiltonian which describes the spin-orbit coupling induced noncrystalline AMR in magnetic materials [34,35]. As described in a phenomenological model, for example, in Refs. [31,36], the longitudinal resistance under magnetic field as a function of current path direction to crystalline direction φ and magnetic field direction θ with respect to the [001] direction of the STO crystal in the plane of the interface could be written as

$$R_{xx}(\theta,\varphi) \approx R_0\{1 + C_I\cos[2(\theta - \varphi)] + C_U\cos(2\theta) + C_C\cos(4\theta) + C_{I,C}\cos[2(\theta+\varphi)]\} \quad (1)$$

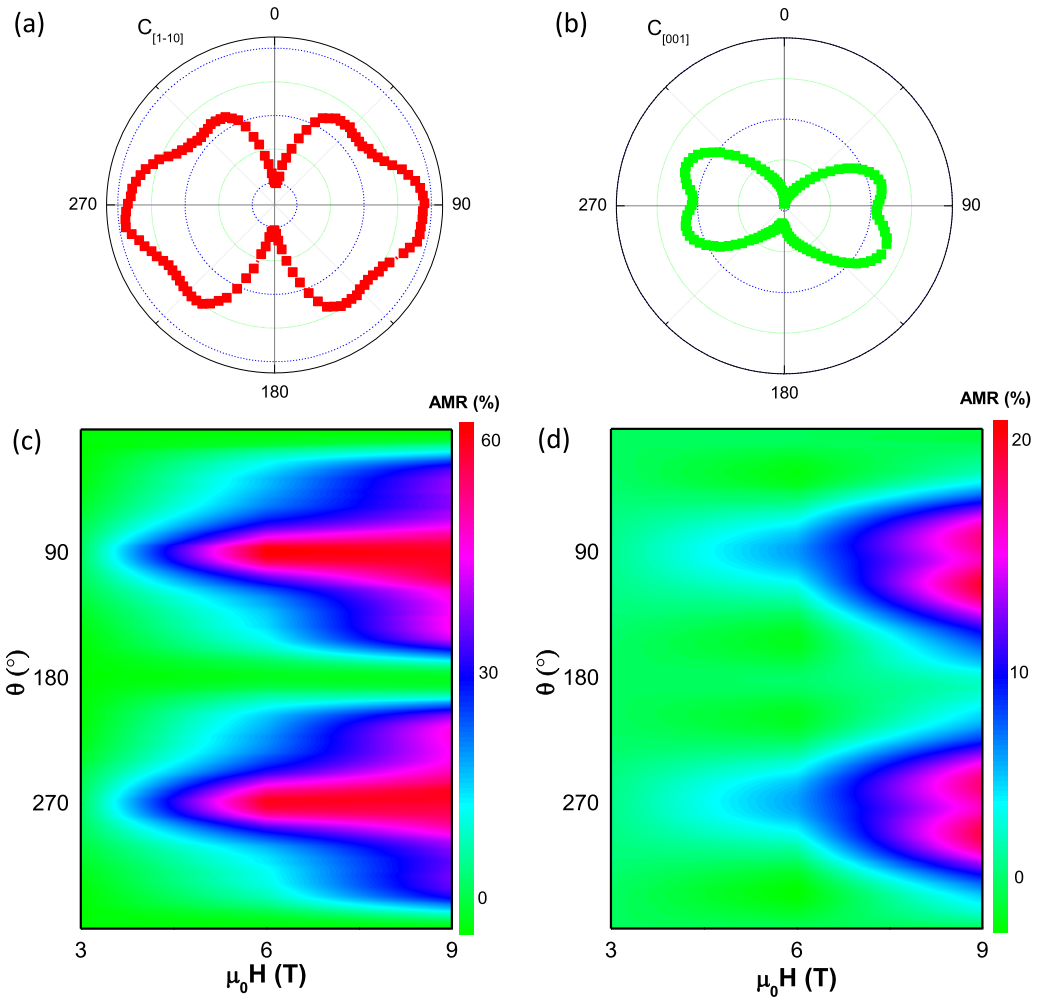

FIG. 3. Comparison of the anisotropic magnetoresistance (AMR) in $[1\bar{1}0]$- and [001]-orientated Hall bars. (a) and (b) Polar plots corresponding to AMR experiments in a 9 T in-plane rotating field and temperature 5 K. The maximum AMR always appears at or close to $[1\bar{1}0]$ direction which is not expected in a normal AMR mechanism contributed by spin-orbit coupling. The AMR of both orientations show violation from $\sin(2\theta)$ behavior and distinct higher harmonic or asymmetric component. (c) and (d) Field-rotation AMR maps demonstrating the AMR contribution moment dominating from $[1\bar{1}0]$ direction.

where the five contributions are the isotropic resistance term, the conventional noncrystalline term, the lowest order uniaxial $[1\bar{1}0]$ and cubic [001] crystalline terms, and a crossed noncrystalline/crystalline term. Noncrystalline AMR depends only on the relative angle between current and magnetization direction or magnetic field. The crossed noncrystalline/crystalline AMR term $C_{I,C}$ depends on the relative angle between current and magnetization direction or magnetic field, the spin-orbit coupling as well as on the magnitude (not direction) of interfacial spin-orbit field, and due to spin-orbit coupling and combining spin-orbit field and magnetism. The crystalline AMR terms C_C and C_U depend on the crystalline anisotropy produced by spin-orbit interaction with the magnetic properties of the system as well as pure orbital effects. In noncrystalline, crystalline, and crossed noncrystalline/crystalline AMR originating from the presence of isotropic spin-orbit interaction, AMR sign flips (the maxima change to minima) when the current direction changes 90°. However, in the presence of strong anisotropic spin-orbit interaction or large anisotropic from pure orbital effect, the AMR sign reserves when one changes the current direction (the maxima and minima do not change), which is a dominant contribution in our observation. We observed a robust maximum in AMR when magnetic field is parallel to the crystalline $[1\bar{1}0]$ direction, independent of the current flow directions [Figs. 2(g) and 2(h)]. Thus, we conclude that an isotropic spin-orbit coupling or spin-orbit field does not lead to the observation, or at least not dominant for the observed giant AMR in LAO/STO(110) systems. The crystal symmetry and strong anisotropic spin-orbit field or orbital effects related crystalline AMR dominates in this (110)-orientated system.

C. Field dependent anisotropic magnetoresistance

We show field sweep AMR $= \{[R(\theta)\text{-}R(0)]/R(0)\} * 100\%$ polar plots comparing the $C_{[1-10]}$ and $C_{[001]}$ case in Figs. 3(a) and 3(b) at 5 K. The observed AMR exhibits a distinct high harmonic or asymmetric component at large fields. This supports the conclusion that crystalline AMR due to wrapping effect on the band structure is related to the crystal symmetries and orbital occupancies discussed by Rushforth *et al.* [31]. Figures 3(c) and 3(d) show field-rotation AMR maps for

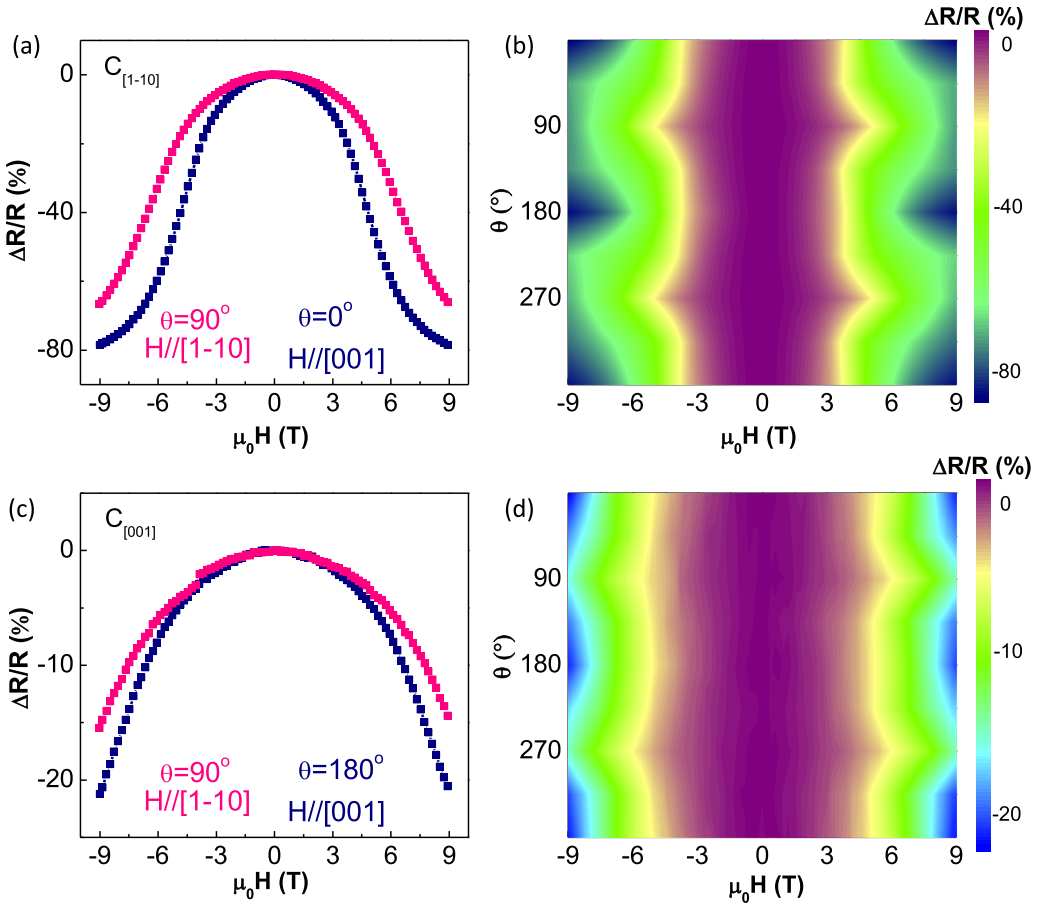

FIG. 4. Field dependent magnetoresistance in $[1\bar{1}0]$- and [001]-orientated Hall bars at 5 K. (a) Magnetoresistance of $[1\bar{1}0]$-orientated Hall bar in applied magnetic field along $\theta = 0^\circ$ and 90°. (b) Field-sweep magnetoresistance map of $[1\bar{1}0]$-orientated Hall bar for the entire range of field angles. (c) Magnetoresistance of [001]-orientated Hall bar in applied magnetic field along $\theta = 0^\circ$ and 90°. (d) Field-sweep magnetoresistance map of [001]-orientated Hall bar for the entire range of field angles.

both $C_{[1-10]}$ and $C_{[001]}$ at 5 K. In the context of a spin-orbit coupling induced AMR scenario in magnetic materials, the magnetization contributing to AMR is dominated by magnetic moment or polarization from [001] direction, which always gives a maxima when the field is along $[1\bar{1}0]$. When the field direction is rotated in the plane, the magnetization direction is almost not disturbed away from hard axis close to [001]. However, the initial direction of magnetization could be altered with increasing magnetic field up to 9 T. The AMR shows mirror symmetry with axis along [001]. In LAO/STO(110) interface, the shape of the orbital is enlarged along [001] direction, whereas it is suppressed along $[1\bar{1}0]$. In this case, the orbital possesses a hybridized d_{xz} and d_{yz} orbital with a shape similar to d_{z^2} orbital, indicating orbital polarization along [001] and orbital hybridization. In the case of $C_{[001]}$, a peak splitting at 7.5 T is observed [Fig. 3(d)]. This peak splitting could be due to an AMR component caused by open orbits as shown in Fig. 5(d), similar to the extra AMR peaks observed by Joshua *et al.* and Ben Shalom *et al.* when electrons occupy d_{xz}/d_{yz} bands [13,30]. One might attribute this to the multibands induced different orbits at the Fermi surface [17,29]. The extra peaks start to appear with applied large magnetic field. This is due to one that can detect the edge of the Brillion zone and the electronic states with large magnetic field. Within the inner side of the Brillion zone, there is only unpolarized d_{xy} band [13], showing a normal AMR, in the presence of a small magnetic field. When the magnetic field is large, the polarized d_{xz}/d_{yz} bands start to play a role and thus lead to extra peaks [13]. We notice that the reconstructed/hybridized orbital shape could be strongly affected by presence of oxygen vacancies (V_O) [37], thus the AMR can be significantly influenced and the position of the maxima in AMR could be somehow shifted (see Fig. 7). The carrier density of the sample is about 2×10^{13} cm^{-2} and mobility is about 350 cm^{2}V^{-1}s^{-1} at 5 K. These are comparable with the previous reports of LAO/STO(110) [14].

Figures 4(a) and 4(c) show field-dependent magnetoresistance (MR) of $C_{[1-10]}$ and $C_{[001]}$ at 5 K with applied magnetic field along $\theta = 0^\circ$ and 90°. While for the $C_{[001]}$ case, the MR shows quadratic behavior up to 9 T, the MR for the $C_{[1-10]}$ case shows quadratic behavior below 3 T, linear in the range between 3 and 6 T, and further increasing the field above 6 T, the slope of MR changes. Previous experimental and theoretical studies have shown that closed orbits produce a ρ_{xx} which saturates as $B \to \infty$ while open orbits produce a ρ_{xx} proportional to B^2 as $B \to \infty$ [38,39] Thus we conclude that closed orbits dominate current flow in the $C_{[1-10]}$ case leading to a saturation around 7 T [Fig. 4(a)], and open orbits dominate current flow in the $C_{[001]}$ case producing a MR $\sim B$

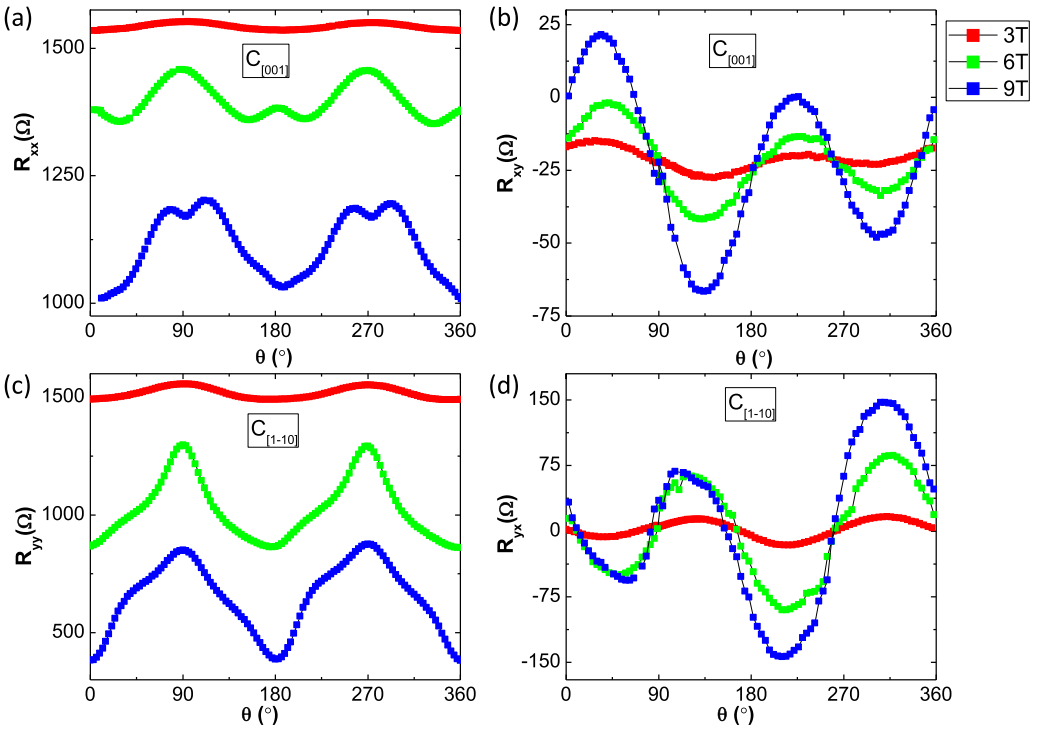

FIG. 5. Longitudinal ADMR $R_{xx}(B,\theta)$ and $R_{yy}(B,\theta)$ and transverse ADMR $R_{xy}(B,\theta)$ and $R_{yx}(B,\theta)$ measurement in an in-plane rotating magnetic field of 3, 6, and 9 T in (a) and (b) [001]-orientated and (c) and (d) [1$\bar{1}$0]-orientated Hall bars with the angles at 5 K. x direction is [001] and y direction is [1$\bar{1}$0].

[2] [Fig. 4(c)]. The closed and open orbits could be seen from the Fermi surface of the system [Fig. 5(c)] and can be related to the splitting of the AMR peak in the $C_{[001]}$ case when the temperature decreases [Fig. 2(h)] or the field increases [Fig. 3(d)], and the orbital induced variable range hopping at low temperature leading to a resistance upturn for the $C_{[1-10]}$ case [Fig. 1(b)] [40].

We also point out that, consistently, the magnitude of $\Delta R(\mu_0 H)/R(0)$ in $C_{[1-10]}$ and $C_{[001]}$ is comparable to that of the corresponding field rotation AMR in LAO/STO(110) (Figs. 4 and 2). Similar experiments to those reported in Figs. 2(a) and 2(b) have been performed over the entire range of angles $0° \leqslant \theta \leqslant 360°$.

D. Angle dependent transverse anisotropic magnetoresistance

In order to determine the complete magnetoresistance tensor $\begin{bmatrix} R_{xx} & R_{xy} \\ R_{yx} & R_{yy} \end{bmatrix}$, we further measure the transverse AMR R_{xy} and R_{yx} shown in Fig. 5. Here x is [001] direction and y is [1$\bar{1}$0] direction. The purely crystalline terms are excluded by symmetry for the transverse AMR [27,28,31]:

$$R_{xy}(\theta,\varphi) = R_0\{C_I \sin[2(\theta-\varphi)] - C_{I,C}\sin[2(\theta+\varphi)] + C_{I,U}\sin[(\theta-\varphi)/2] - C_{U,C}\sin[(\theta+\varphi)/2]\} \quad (2)$$

The maximum of R_{xy} appears when the angle between magnetic field and current direction equals $\pi/4$ and the minimum appears at $3\pi/4$ for current along [001]. The maximum of R_{xy} shifts by $\pi/2$ for current along [1$\bar{1}$0]. This shows that the spin-orbit field or spin-orbit coupling related AMR changes with the current direction as shown in Figs. 5(b) and 5(d). In contrast to the normal spin-orbit related AMR, the strong spin-orbit field or orbital effect dominated AMR [41,42] does not rotate with the current direction as shown in Figs. 5(a) and 5(c), as well as in Figs. 1–4. We could further see that the R_{xy} increases faster for current along [1$\bar{1}$0] with a polar direction indicating nonsymmetrical orbital polarization than for current along [001]. However, the changes of R_{xy} are much less than the changes of R_{xx} and the magnitude is similar as the noncrystalline dominated AMR in LAO/STO(001) [14]. Usually the planner Hall effect R_{xy} originating from AMR is rather small, for example, 0.22% in $Co_{60}Fe_{20}B_{20}$ [43]. This further confirms the large orbital effect in transport properties of LAO/STO(110) systems. We note there is a nonzero residual R_{xy} about $-22\ \Omega$ for current along [001] direction while it is absent for current along [1$\bar{1}$0].

The change of R_{xx}, R_{yy} is about 200 Ω (∼20 % AMR) and 480 Ω (∼60 % AMR) at 5 K and 9 T in Figs. 5(a) and 5(c), respectively. The change of R_{xy}, R_{yx} is about 88 and 290 Ω at 5 K and 9 T, respectively [Figs. 5(b) and 5(d)]. Instead, in (001)-orientated LAO/STO, for example, we take the value in Ref. [13], the change of R_{xx} is about 60 Ω (∼4 % AMR) for a low carrier density sample and 10 Ω (∼20 % AMR) for high carrier density samples at 2 K and 14 T, respectively (Fig. 1 in Ref. [13]), and the change of R_{xy} is about 60 Ω for low carrier density samples and 20 Ω for a low carrier density sample at 2 K and 14 T, respectively (Fig. 1 in Ref. [13]), the largest value is about 100 Ω in Ref. [14]. An important feature we should notice is that $R_{xy} \neq R_{yx}$ in (110) case. Comparing the observed magnetoresistance tensor to (001)-orientated LAO/STO, we could infer that a strong anisotropic spin-orbit field related to an anisotropic Fermi surface is the dominant mechanism in the observed giant crystalline AMR [30,41].

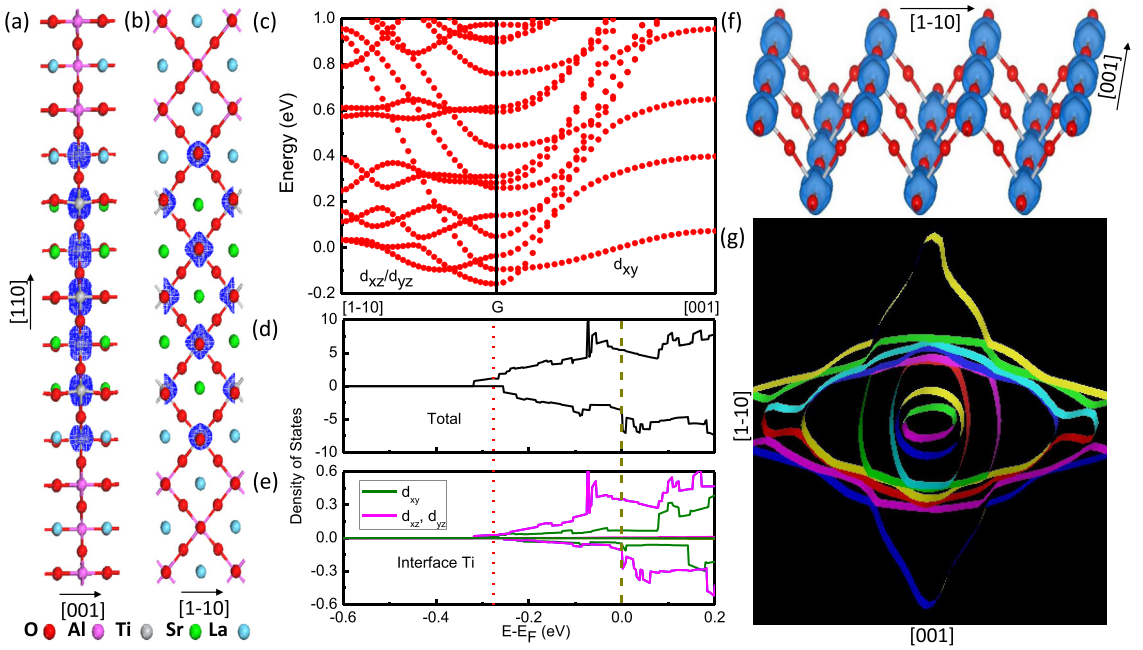

FIG. 6. Hybridized and polarized orbitals in LAO/STO(110) heterostructures calculated by DFT, spatial charge distribution, and Fermi surface of LAO/STO(110) heterostructure. Structural guidance for the model of LAO/STO(110) with spatial charge distribution along [001] (a) and along [1$\bar{1}$0] (b). (c) Electronic band structure of LAO/STO(110). (d) and (e) The calculated total and interfacial density of states. (f) Charge density distribution at interfacial TiO_2 layer of LAO/STO(110). (g) Calculated Fermi surface of the LAO/STO(110) in (110) plane.

The observed R_{xy} data are complicated. It seems that there is rotation symmetry broken in this system which deserves further investigation. This complicated R_{xy} data might be related to C_{2v} symmetry in this system. This calls for an open question of the relation between the crystal structure, Fermi surface, and spin-orbit order in this system which might further stimulate more interesting work later on.

The maximum crystalline AMR observed in LAO/STO(110) can vary between 57% and 104% for different samples with different P_{O2}, which could be understood that the presence of oxygen vacancies could significantly affect the reconstructed orbital shape [37]. In general, however, the AMR is significantly larger (approximately more than 10 to 20 times) compared to that obtained in magnetic materials which is only around several percents [31]. Moreover, the crystalline AMR shows a resistivity maximum when magnetic field is along [1$\bar{1}$0], independent of the current direction, though it is larger for current along [1$\bar{1}$0] than [001]. This implies that the observed AMR is dominated by a crystalline component.

IV. ANALYSIS AND DISCUSSION

A. Orbital polarization, hybridization, and ordering

In order to understand the origin of this giant crystalline AMR, density functional theory (DFT) calculations have been performed. The result suggests that the origin of the giant crystalline AMR is due to the orbital reconstruction induced orbital polarization at the LAO/STO(110) interface and the corresponding anisotropic electronic structure. The effective mass and energy of electrons at d_{xz}/d_{yz} and d_{xy} orbitals are very different in LAO/STO(110) [22,23], compared to those in the (001) case [9,13]. Figures 6(a) and 6(b) show the DFT model of LAO/STO(110) and the spatial charge distribution along [001] and [1$\bar{1}$0], respectively. Interestingly, it is found that the spatial charge distribution in (110) plane forms a hybridized d_{xz} and d_{yz} orbital along [001], especially at the interface. The energy level is reversed with d_{xz}/d_{yz} at the lowest energy states compared to (001) interface [Figs. 6(c)–6(e)]. Along [1$\bar{1}$0], the spatial charge distribution is more uniform. This result confirms that orbital polarization and hybridization occurs along [001] at the interface of the LAO/STO(110) shown in Fig. 6(f), leading to unique Fermi surface and open/closed orbit along a different direction [Fig. 6(g)]. It can be seen clearly that the band structure along [1$\bar{1}$0] is different from that of along [001]. Therefore, the effective mass is different along [001] and [1$\bar{1}$0] in LAO/STO(110) interfaces, which is also different from that of LAO/STO(001) interfaces. It is found that the orbitals hybridize and polarize along [001] direction at the interface. This unique orbital configuration and Fermi surface with open and closed orbits is responsible for the giant crystalline AMR in the LAO/STO(110) interface. Unique surface structure in LAO/STO(110) leads to orbital energy reversal and orbital hybridization. The dominating orbital states are now d_{xz}/d_{yz} with the lowest energy state in contrast to d_{xy} in LAO/STO(001). Furthermore, the Fermi surface reconstructs in the (110) case as shown in Figs. 6(g). All these result in the observed anomalous AMR behavior. Previous works have also shown that the details of the Fermi surface play a more important role in determining the AMR behavior than the scattering process in the case $\omega_c\tau$ is larger than 1 where ω_c is cyclotron frequency and τ is relaxation time [20]. In fact, a large negative in-plane MR effect above the superconducting transition appearing in LAO/STO(001) could be explained from a point of view of combination effect of

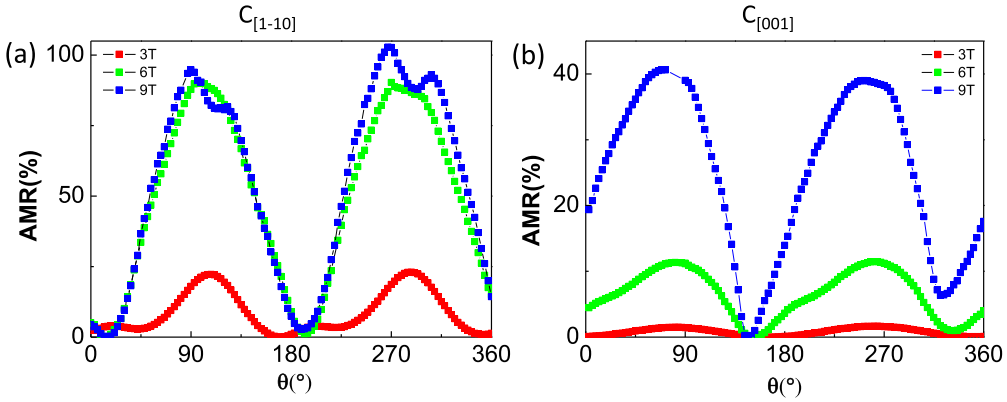

FIG. 7. AMR up to 104% observed in 10 unit cells LAO/STO(110) sample grown at oxygen partial pressure of 5×10^{-5} Torr. Magnetoresistance measurement in an in-plane rotating magnetic field of 3, 6, and 9 T in (a) [1$\bar{1}$0]-orientated and (b) [001]-orientated Hall bars with the angles.

spin-orbit coupling and scattering from finite-range impurities, which might be due to a highly anisotropic deformation of the Fermi surface and strong interband scattering changed externally such as by electric field [10,44]. In the (110) case, the band becomes strongly hybridized and polarized, thus an external electric field does not easily influence the electronic properties including the electric effect on the resistance, carrier density, and superconducting transition temperature as the (001) case [17]. This indicates that the spin-orbit coupling might play an important role for onset of the superconducting transition. An anomalous AMR effect also occurs close to the metal-insulator transition in perovskite manganite [44], showing a direct correlation with the anisotropic field-tuned metal-insulator transition in the system. A small crystalline anisotropy stimulates a "colossal" AMR near the transition phase boundary of the perovskite manganite system, which reveals there are interplay between magneto- and electronic-crystalline couplings close to metal-insulator transition. This might be similar to the case close to the superconducting transition in LAO/STO that the interplay between magneto- and electronic-crystalline couplings starts to play a role [44,45].

These distinct properties might help to understand the very different electronic properties in (001)- and (110)-orientated systems. There are reports about superconducting transition along different crystalline directions at 100–200 mK temperature range. It has been observed a lower onset temperature of superconducting transition for (110)-orientated interface (see for example Ref. [17]). The transition temperature along [1$\bar{1}$0] is also lower compared to [001] direction current both from resistance vs temperature and IV curve measurement in (110) systems [46]. In fact, we have shown in Fig. 1(d) that the resistance upturns at low temperature due to orbital hopping along zigzag [1$\bar{1}$0] Ti-O-Ti chains. There is a relation between large MR/AMR effect and superconducting pairing mechanism since they are both based on strong anisotropic spin-orbit coupling at the interface. We argue that the superconductivity is related to d orbital electrons pairing preserved by strong spin-orbit coupling at the interface [44,47]. Rashba spin-orbit coupling has been shown to be larger in the d_{xz}/d_{yz} bands than that observed in the d_{xy} bands. The strong anisotropic spin-orbit coupling at the interface preserves pairing in the d_{xz} and d_{yz} bands with a larger effective mass along [1$\bar{1}$0] with a lower transition temperature than [001] in (110) interface [48]. d_{xy} orbitals are less polarized with smaller spin-orbit coupling than d_{xz}/d_{yz}, thus d_{xy} orbitals are more sensitive to external electric field as the gating modulation of superconducting state in (110) interface compared to (001). This could be understood from gating modulation of superconducting state in (110)-orientated interface compared with (001)-orientated interface [17].

B. Enhancement of orbital polarization along [001] by oxygen vacancies

We note the crystalline AMR induced by orbital effect could be greatly enhanced by introducing interfacial oxygen vacancies (Fig. 7 and Table I). This could be easily understood since oxygen vacancies can largely enhance orbital polarization [37]. This is confirmed by DFT calculation with oxygen vacancies at the surface or at the interface shown in Fig. 8. The presence of the oxygen vacancies at the interface greatly enlarges the reconstructed orbital shape along [001] direction as shown in Fig. 8(a). This leads to extremely large contribution to the crystalline AMR from orbital effects up to 104% which is not reported or observed in other systems or in (001)-orientated LAO/STO system (Fig. 7 and Table I). Though the crystalline AMR has been observed in many systems and they dominate in some cases, however, their magnitude is much smaller than what we observe, usually below 1% (0.1% in (In,Fe)As ferromagnetic semiconductor [49], 0.4% in quasi-2D Fe on GaAs [47], 2%–3% in quaternary ferromagnetic semiconductor (Ga,Mn)(As,Sb) [27]). However, this "crystalline" AMR due to orbital shape might not always be along the crystalline axes as it strongly depends on the shape of the orbitals. In the presence of the orbital hybridization, for example, induced by varying oxygen vacancies or in presence of splitting induced by large magnetic field, the orbital shapes might change, which instead leads to a crystalline AMR slightly deviating from the crystalline axes. There will be relative changes of population of d_{yz}/d_{xz} orbital and d_{xy} orbital electrons due to carrier density change when one changes oxygen partial pressure in the LAO deposition procedure, thus there will also be corresponding changes of topology of Fermi surface. The change of topology of Fermi surface would lead to the different spin-orbit field situations and different AMR effect both on amplitude and the

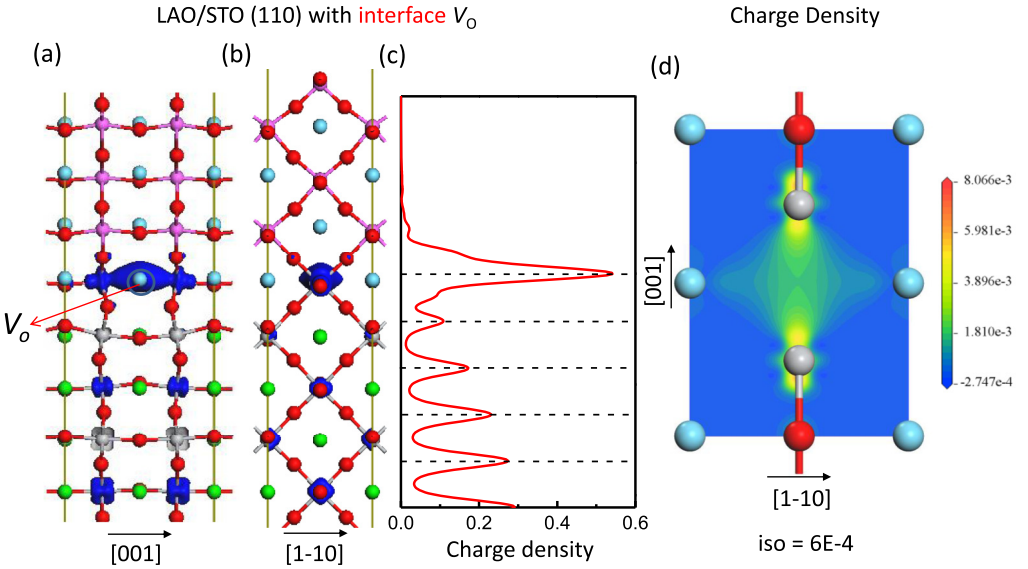

FIG. 8. Charge density distribution and density of states in LAO/STO(110) heterostructures with interface oxygen vacancy calculated by DFT. Structural guidance for the model of LAO/STO(110) with spatial charge distribution along [001] (a) and along [1$\bar{1}$0] (b). (c) Calculated total charge density of the LAO/STO(110). (d) Charge density of the LAO/STO(110) in the interface plane (110).

position of the maximum. This issue would be interesting for further study.

C. Anisotropic spin-orbit field induced by unique Fermi surface

To understand the origin of the giant crystalline AMR in the context of spin-orbit coupling, a strong anisotropic spin-orbit interaction within LAO/STO(110) along different crystalline axes is necessary to consider [17,50]. The effective mass of d_{xz}/d_{yz} electrons occupying the lowest energy states is different by more than one order of magnitude between [001] and [1$\bar{1}$0] direction, about 0.6 and 6 electron mass, respectively [16]. The corresponding Fermi surface is also very anisotropic as schematically shown in Fig. 9. The impressive feature shown in Fig. 6(c) is that the electronic band with lowest carrier density only occupying the d_{xz}/d_{yz} orbitals is degenerate, thus behaving as a single band system which is not possible in (001)-orientated system which has different subbands even for d_{xy} state. In the presence of large magnetic fields, d_{xz}/d_{yz} states are not degenerate any more [Fig. 9(d)], leading to a peak in AMR as shown in Figs. 2, 5, and 7. Increasing carrier density by introducing oxygen vacancies leads to pronounced giant AMR behavior as shown in Fig. 7 since the anisotropy is enhanced with larger carrier density. Based on this model, we could fit the main feature of our data shown in Fig. 10. Note we have included AMR terms due to C_{2v} symmetry in the system

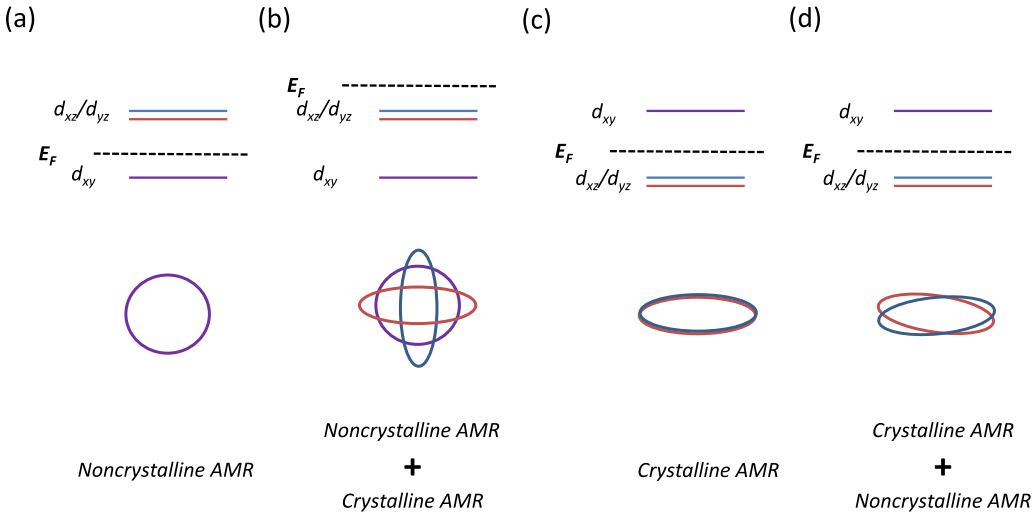

FIG. 9. Origin of the noncrystalline and crystalline AMR in LAO/STO. (a) LAO/STO(001) with carrier density n below the critical value n_c. (b) LAO/STO(001) with carrier density n above the critical value n_c. (c) LAO/STO(110) with Fermi energy only occupying the degenerate lowest energy states d_{xz}/d_{yz}. (d) LAO/STO(110) with Fermi energy only occupying the undegenerate lowest energy states d_{xz}/d_{yz} (for example splitting with large magnetic field).The top row is a scheme of energy level in t_{2g} state with d_{xy} and d_{xz}/d_{yz} orbitals and the location of the Fermi energy. The second row is a scheme of Fermi surface at the Fermi energy. The bottom row is an AMR component.

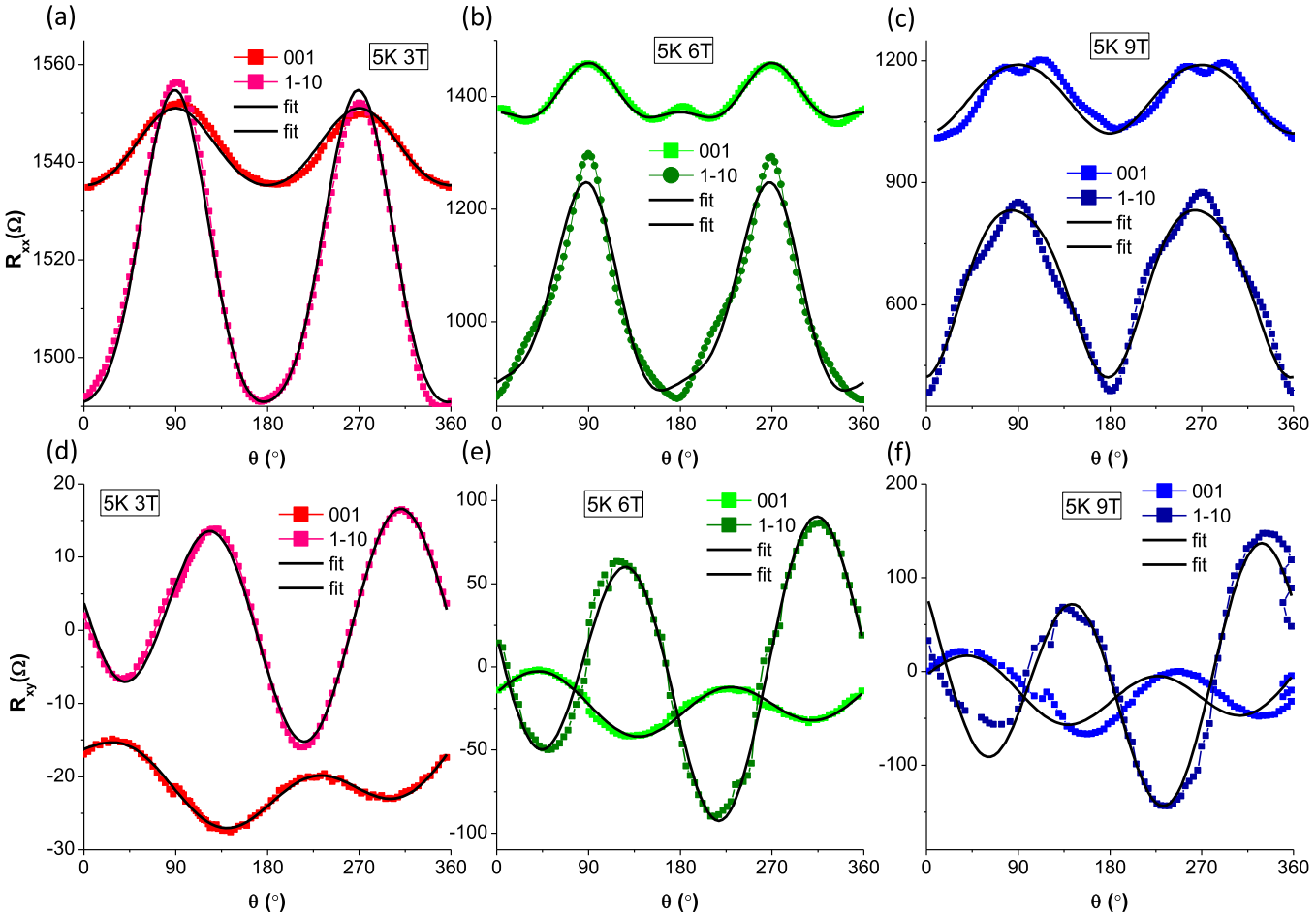

FIG. 10. Fitting of the (a)–(c) longitudinal and (d)–(f) transverse AMR to anisotropic AMR model. (a) and (d) 3 T, (b) and (e) 6 T, and (c) and (f) 9 T.

in the fitting Eq. (2). The information from fitting we could obtain is that the crystalline contribution from [001] orientation is about two orders of magnitude larger than [1$\bar{1}$0] (Table II), which is consistent with our picture in Figs. 9(c) and 9(d). We could find that the fitting is good for low field, however, the simple model is not fitting well for large fields since there are additional contributions from multibands, Zeeman splitting, and other origins such as impurities scattering. The exact relation between anisotropic spin-orbit field and anisotropic Fermi surface, anisotropic Coulomb interaction, and crystal field deserves further theoretical study [51,52].

TABLE II. Fitting parameters obtained in Fig. 10. The most important information is the relative value C_I/C_U which characterizes the anisotropy along [001] and [1$\bar{1}$0] direction.

Hall bar \ Sample		C_I	C_U	C_C	$C_{I,C}$
$C_{[001]}$	3 T	0.00230	0.00052	0.00230	0.00230
	6 T	0.00302	0.00030	0.00302	0.00598
	9 T	0.00371	0.00646	0.00371	0.00371
$C_{[1-10]}$	3 T	4.69750	7.14×10^{-5}	1.33300	3.36110
	6 T	6.16700	4.20×10^{-5}	1.33280	4.80000
	9 T	6.10645	3.00×10^{-5}	1.33500	4.77295

V. CONCLUDING REMARKS

Note that we have to clarify that we did not claim the origin of the giant AMR is the existence of magnetic order as our MR data showed no hysteresis. The existence of spin-orbit interaction is sufficient for the appearance of AMR, which forms the basis for our explanation of the observed giant AMR effect. In our proposed mechanism to explain this giant crystalline AMR in Fig. 9, we have shown that the anisotropic Fermi surface leads to strong anisotropic spin-orbit coupling (as well as effective mass) leading to the observed effect. Even though the existence of magnetic order was not a prerequisite condition for appearance of giant crystalline AMR, in many other cases magnetic order is crucial for other different types of AMRs.

The unique symmetry of LAO/STO(110) leads to orbital reconstruction induced orbital polarization and ordering, which results in the anisotropic band structure and Fermi surface [Fig. 6(g)]. This orbital polarization, ordering, and hybridization leads to both open and closed orbits along [001] direction and only closed orbits along [1$\bar{1}$0] direction in LAO/STO(110) interface as shown in Fig. 6(d). (Note that LAO plays an important role to induce this open orbits along [001] direction as we do not have open orbits for STO(110) system.) The giant crystalline AMR signal observed in LAO/STO(110) is due to the anisotropic spin-orbit coupling

induced by interfacial Ti orbitals. It is known that orbital polarization effects can strongly enhance the magnetic anisotropy energy in low-dimensional systems [53–55], and are of particular importance for this interpretation since a Stoner-like Hamiltonian [56] fails to reproduce the experimental results. Giant crystalline anisotropic magnetoresistance observed in LAO/STO(110) is due to highly anisotropic reconstructed orbitals induced scatterings which have a maximum when magnetic field is along $[1\bar{1}0]$, namely, the field is perpendicular to the orbital polarization direction [001], independent of the current flow direction. This orbital polarization induces very unique band structure in LAO/STO(110), especially along $[1\bar{1}0]$, with partially flat subbands and open orbits along [001] direction and elliptical Fermi surface, leading to the giant crystalline AMR, which also provides new opportunity for single band physics and orbital physics [57], magnetic recording technologies, and even ultrasensitive magnetometer for biomagnetic fields [58].

ACKNOWLEDGMENTS

We gratefully acknowledge helpful discussions with Q. F. Zhang, S. Yunoki, and Z. C. Zhong. We thank the Singapore National Research Foundation (NRF) under the Competitive Research Programs (CRP Awards No. NRF-CRP10-2012-02 and No. NRF-CRP15-2015-01) and the NUS FRC (AcRF Tier 1 Grants No. R-144-000-346-112 and No. R-144-000-364-112).

[1] A. Ohtomo and H. Y. Hwang, A high-mobility electron gas at the $LaAlO_3/SrTiO_3$ heterointerface, Nature (London) **427**, 423 (2004).

[2] N. Reyren *et al.*, Superconducting interfaces between insulating oxides, Science **317**, 1196 (2007).

[3] A. Brinkman *et al.*, Magnetic effects at the interface between non-magnetic oxides, Nat. Mater. **6**, 493 (2007).

[4] Ariando *et al.*, Electronic phase separation at the $LaAlO_3/SrTiO_3$ interface, Nat. Commun. **2**, 188 (2011).

[5] D. A. Dikin, M. Mehta, C. W. Bark, C. M. Folkman, C. B. Eom, and V. Chandrasekhar, Coexistence of Superconductivity and Ferromagnetism in Two Dimensions, Phys. Rev. Lett. **107**, 056802 (2011).

[6] J. A. Bert *et al.*, Direct imaging of the coexistence of ferromagnetism and superconductivity at the $LaAlO_3/SrTiO_3$ interface, Nat. Phys. **7**, 767 (2011).

[7] L. Li, C. Richter, J. Mannhart, and R. C. Ashoori, Coexistence of magnetic order and two-dimensional superconductivity at $LaAlO_3/SrTiO_3$ interfaces, Nat. Phys. **7**, 762 (2011).

[8] F. Bi *et al.*, Room-temperature electronically-controlled ferromagnetism at the $LaAlO_3/SrTiO_3$ interface, Nat. Commun. **5**, 5019 (2014).

[9] J.-S. Lee *et al.*, Titanium d_{xy} ferromagnetism at the $LaAlO_3/SrTiO_3$ interface, Nat. Mater. **12**, 703 (2013).

[10] A. D. Caviglia, M. Gabay, S. Gariglio, N. Reyren, C. Cancellieri, and J.-M. Triscone, Tunable Rashba Spin-Orbit Interaction at Oxide Interfaces, Phys. Rev. Lett. **104**, 126803 (2010).

[11] M. Ben Shalom, M. Sachs, D. Rakhmilevitch, A. Palevski, and Y. Dagan, Tuning Spin-Orbit Coupling and Superconductivity at the $SrTiO_3/LaAlO_3$ Interface: A Magnetotransport Study, Phys. Rev. Lett. **104**, 126802 (2010).

[12] P. D. C. King *et al.*, Quasiparticle dynamics and spin-orbital texture of the $SrTiO_3$ two-dimensional electron gas, Nat. Commun. **5**, 3414 (2014).

[13] A. Joshua, J. Ruhman, S. Pecker, E. Altman, and S. Ilani, Gate-tunable polarized phase of two-dimensional electrons at the $LaAlO_3/SrTiO_3$ interface, Proc. Natl. Acad. Sci. USA **110**, 9633 (2013).

[14] A. Annadi *et al.*, Anisotropic two-dimensional electron gas at the $LaAlO_3/SrTiO_3$ (110) interface, Nat. Commun. **3**, 1838 (2013).

[15] G. Herranz, F. Sánchez, N. Dix, M. Scigaj, and J. Fontcuberta, High mobility conduction at (110) and (111) $LaAlO_3/SrTiO_3$ interfaces, Sci. Rep. **2**, 758 (2012).

[16] Z. M. Wang *et al.*, Anisotropic two-dimensional electron gas at $SrTiO_3$(110), Proc. Natl. Acad. Sci. USA **111**, 3933 (2014).

[17] G. Herranz *et al.*, Engineering two-dimensional superconductivity and Rashba spin-orbit coupling in $LaAlO_3/SrTiO_3$ quantum wells by selective orbital occupancy, Nat. Commun. **6**, 6028 (2015).

[18] A. Annadi, Z. Huang, K. Gopinadhan, X. Renshaw Wang, A. Srivastava, Z. Q. Liu, H. Harsan Ma, T. P. Sarkar, T. Venkatesan, and Ariando, Fourfold oscillation in anisotropic magnetoresistance and planar Hall effect at the $LaAlO_3/SrTiO_3$ heterointerfaces: Effect of carrier confinement and electric field on magnetic interactions, Phys. Rev. B **87**, 201102(R) (2013).

[19] S. Seri, E. Shimshoni, S. Paetel, J. Mannhart, and L. Klein, Angular dependence of the magnetoresistance of the $SrTiO_3/LaAlO_3$ interface, IEEE Trans. Mag. **46**, 1630 (2010).

[20] Q. Li, B. T. Liu, Y. F. Hu, J. Chen, H. Gao, L. Shan, H. H. Wen, A. V. Pogrebnyakov, J. M. Redwing, and X. X. Xi, Large Anisotropic Normal-State Magnetoresistance in Clean MgB_2 Thin Films, Phys. Rev. Lett. **96**, 167003 (2006).

[21] H. J. H. Ma, Z. Huang, W. M. Lü, A. Annadi, S. W. Zeng, L. M. Wong, S. J. Wang, T. Venkatesan, and Ariando, Tunable bilayer two-dimensional electron gas in $LaAlO_3/SrTiO_3$ superlattices, Appl. Phys. Lett. **105**, 011603 (2014).

[22] W. Thomson, On the electro-dynamic qualities of metals: Effects of magnetization on the electric conductivity of nickel and of iron, Proc. R. Soc. London **8**, 546 (1857).

[23] I. A. Campbell, A. Fert, and O. Jaoul, The spontaneous resistivity anisotropy in Ni-based alloys, J. Phys. C **3**, S95 (1970).

[24] P. Wisniewski, Giant anisotropic magnetoresistance and magnetothermopower in cubic 3:4 uranium pnictides, Appl. Phys. Lett. **90**, 192106 (2007).

[25] W. Döring, Die abhängigkeit des widerstandes von nickelkristallen von der Richtung der spontanen magnetisierung, Ann. Phys. (Leipzig) **424**, 259 (1938).

[26] R. P. van Gorkom, J. Caro, T. M. Klapwijk, and S. Radelaar, Temperature and angular dependence of the anisotropic magnetoresistance in epitaxial Fe films, Phys. Rev. B **63**, 134432 (2001).

[27] B. Howells, M. Wang, K. W. Edmonds, P. Wadley, R. P. Campion, A. W. Rushforth, C. T. Foxon, and B. L. Gallagher, Crystalline anisotropic magnetoresistance in quaternary ferromagnetic semiconductor (Ga,Mn)(As,Sb), Appl. Phys. Lett. **102**, 052407 (2013).

[28] J. Li, S. L. Li, Z. W. Wu, S. Li, H. F. Chu, J. Wang, Y. Zhang, H. Y. Tian, and D. N. Zheng, A phenomenological approach to the anisotropic magnetoresistance and planar Hall effect in tetragonal $La_{2/3}Ca_{1/3}MnO_3$ thin films, J. Phys. Condens. Matter **22**, 146006 (2010).

[29] M. Salluzzo, J. C. Cezar, N. B. Brookes, V. Bisogni, G. M. De Luca, C. Richter, S. Thiel, J. Mannhart, M. Huijben, A. Brinkman, G. Rijnders, and G. Ghiringhelli, Orbital Reconstruction and the Two-Dimensional Electron Gas at the $LaAlO_3/SrTiO_3$ Interface, Phys. Rev. Lett. **102**, 166804 (2009).

[30] M. Ben Shalom, C. W. Tai, Y. Lereah, M. Sachs, E. Levy, D. Rakhmilevitch, A. Palevski, and Y. Dagan, Anisotropic magnetotransport at the $SrTiO_3/LaAlO_3$ interface, Phys. Rev. B **80**, 140403 (2009).

[31] A. W. Rushforth, K. Výborný, C. S. King, K. W. Edmonds, R. P. Campion, C. T. Foxon, J. Wunderlich, A. C. Irvine, P. Vašek, V. Novák, K. Olejník, Jairo Sinova, T. Jungwirth, and B. L. Gallagher, Anisotropic Magnetoresistance Components in (Ga,Mn)As, Phys. Rev. Lett. **99**, 147207 (2007).

[32] H. J. H. Ma, S. Scharinger, S.W. Zeng, D. Kohlberger, M. Lange, A. Stöhr, X. R. Wang, T. Venkatesan, R. Kleiner, J. F. Scott, J. M. D. Coey, D. Koelle, and Ariando, Local Electrical Imaging of Tetragonal Domains and Field-Induced Ferroelectric Twin Walls in Conducting $SrTiO_3$, Phys. Rev. Lett. **116**, 257601 (2016).

[33] Y. Frenkel, N. Haham, Y. Shperber, C. Bell, Y. W. Xie, Z. Y. Chen, Y. Hikita, H. Y. Hwang, and B. Kalisky, Anisotropic transport at the $LaAlO_3/SrTiO_3$ interface explained by microscopic imaging of channel-flow over $SrTiO_3$ domains, ACS Appl. Mater. Interfaces **8**, 12514 (2016).

[34] T. Jungwirth, J. Sinova, J. Mašek, J. Kučera, and A. H. MacDonald, Theory of ferromagnetic (III,Mn)V semiconductors, Rev. Mod. Phys. **78**, 809 (2006).

[35] T. Dietl, H. Ohno, and F. Matsukura, Hole-mediated ferromagnetism in tetrahedrally coordinated semiconductors, Phys. Rev. B **63**, 195205 (2001).

[36] T. Hupfauer, A. Matos-Abiague, M. Gmitra, F. Schiller, J. Loher, D. Bougeard, C. H. Back, J. Fabian, and D. Weiss, Emergence of spin-orbit fields in magnetotransport of quasi-two-dimensional iron on gallium arsenide, Nat. Commun. **6**, 7374 (2015).

[37] N. Pavlenko, T. Kopp, E. Y. Tsymbal, J. Mannhart, and G. A. Sawatzky, Oxygen vacancies at titanate interfaces: Two-dimensional magnetism and orbital reconstruction, Phys. Rev. B **86**, 064431 (2012).

[38] F. Batallan and I. Rosenman, Magnetoresistance and open orbits domain in cobalt, Solid State Commun. **12**, 75 (1973).

[39] E. Fawcett and W. A. Reed, Multiple Connectivity of the Fermi Surface of Nickel from its Magnetoresistance Anisotropy, Phys. Rev. Lett. **9**, 336 (1962).

[40] U. Sivan, O. Entin-Wohlman, and Y. Imry, Orbital Magnetoconductance in the Variable-Range–Hopping Regime, Phys. Rev. Lett. **60**, 1566 (1988).

[41] F. F. Balakirev, I. E. Trofimov, S. Guha, M. Z. Cieplak, and P. Lindenfeld, Orbital magnetoresistance in the $La_{2-x}Sr_xCuO_4$ system, Phys. Rev. B **57**, R8083(R) (1998).

[42] A. Collaudin, B. Fauqué, Y. Fuseya, W. Kang, and K. Behnia, Angle Dependence of the Orbital Magnetoresistance in Bismuth, Phys. Rev. X **5**, 021022 (2015).

[43] K. M. Seemann, F. Freimuth, H. Zhang, S. Blugel, Y. Mokrousov, D. E. Burgler, and C. M. Schneider, Origin of the Planar Hall Effect in Nanocrystalline $Co_{60}Fe_{20}B_{20}$, Phys. Rev. Lett. **107**, 086603 (2011).

[44] M. Diez, A. M. R. V. L. Monteiro, G. Mattoni, E. Cobanera, T. Hyart, E. Mulazimoglu, N. Bovenzi, C. W. J. Beenakker, and A. D. Caviglia, Giant Negative Magnetoresistance Driven by Spin-Orbit Coupling at the $LaAlO_3/SrTiO_3$ Interface, Phys. Rev. Lett. **115**, 016803 (2015).

[45] R.-W. Li, H. B. Wang, X. W. Wang, X. Z. Yu, Y. Matsui, Z.-H. Cheng, B.-G. Shen, E. W. Plummere, and J. D. Zhang, Anomalously large anisotropic magnetoresistance in a perovskite manganite, PNAS **106**, 14224 (2009).

[46] APS March Meeting 2016, abstract E30.006 and private communication.

[47] K. Michaeli, A. C. Potter, and P. A. Lee, Superconducting and Ferromagnetic Phases in $SrTiO_3/LaAlO_3$ Oxide Interface Structures: Possibility of Finite Momentum Pairing, Phys. Rev. Lett. **108**, 117003 (2012).

[48] G. G. N. Angilella, N. H. March, and R. Pucci, T_c for non-s-wave pairing superconductors correlated with coherence length and effective mass, Phys. Rev. B **62**, 13919 (2000).

[49] P. N. Hai, D. Sasaki, L. D. Anh, and M. Tanaka, Crystalline anisotropic magnetoresistance with two-fold and eight-fold symmetry in (In,Fe)As ferromagnetic semiconductor, Appl. Phys. Lett. **100**, 262409 (2012).

[50] K. Gopinadhan, A. Annadi, Y. Kim, A. Srivastava, B. Kumar, J. S. Chen, J. M. D. Coey, Ariando, and T. Venkatesan, Gate tunable in- and out-of-plane spin-orbit coupling and spin-splitting anisotropy at $LaAlO_3/SrTiO_3$ (110) interface, Adv. Electr. Matters **1**, 1500114 (2015).

[51] G. R. Zhang, E. Gorelov, E. Sarvestani, and E. Pavarini, Fermi Surface of Sr_2RuO_4: Spin-Orbit and Anisotropic Coulomb Interaction Effects, Phys. Rev. Lett. **116**, 106402 (2016).

[52] R. Skomski, A. Kashyap, and A. Enders, Is the magnetic anisotropy proportional to the orbital moment?, J. Appl. Phys. **109**, 07E143 (2011).

[53] M. Bode *et al.*, Chiral magnetic order at surfaces driven by inversion asymmetry, Nature (London) **447**, 190 (2007).

[54] G. Autès, C. Barreteau, M. C. Desjonquères, D. Spanjaard, and M. Viret, Giant orbital moments are responsible for the anisotropic magnetoresistance of atomic contacts, Europhys. Lett. **83**, 17010 (2008).

[55] H. Capellmann, Theory of itinerant ferromagnetism in the 3-d transition metals, Z. Phys. B Condens. Matter **34**, 29 (1979).

[56] M. E. A. Coury, S. L. Dudarev, W. M. C. Foulkes, A. P. Horsfield, P.-W. Ma, and J. S. Spencer, Hubbard-like Hamiltonians for interacting electrons in s, p, and d orbitals, Phys. Rev. B **93**, 075101 (2016).

[57] Y. Tokura and N. Nagaosa, Orbital physics in transition-metal oxides, Science **288**, 462 (2000).

[58] I. Tominec, E. Breznik, A. Titorič, and S. Penič, Application of anisotropic magnetoresistive sensors for detection of changes in organ activity; D. Belavič and I. Šorli (Ljubljana MIDEM - Society for Microelectronics, Electronic Components and Materials, Slovenia, 2012), http://elektronika-start.com/wp-content/uploads/2012/09/Application-of-Anisotropic-Magnetoresistive-sesnsors-for.pdf.